

Radiologic-Pathologic Analysis of Increased Ethanol Localization and Ablative Extent Achieved by Ethyl Cellulose

Erika Chelales (✉ erika.chelales@duke.edu)

Duke University

Robert Morhard

Duke University

Corrine Nief

Duke University

Brian Crouch

Duke University

Alan Sag

Duke Medical Center

Nirmala Ramanujam

Duke University

Research Article

Keywords: radiodensity, ethanol concentration-radiodensity, ethanol

Posted Date: December 4th, 2020

DOI: <https://doi.org/10.21203/rs.3.rs-115251/v1>

License: © ⓘ This work is licensed under a Creative Commons Attribution 4.0 International License.

[Read Full License](#)

Abstract

Purpose

Ethanol provides a rapid, low-cost ablative solution for liver tumors with a small technological footprint but suffers from uncontrolled diffusion in target tissue, limiting treatment precision and accuracy. The authors demonstrate that incorporating the gel-forming polymer ethyl cellulose to ethanol localizes the distribution. This therapy may have a low barrier of entry for cancer care in low- and middle- income countries.

Materials and Methods

The relationship of radiodensity to ethanol concentration was characterized with water-ethanol surrogates. *Ex vivo* EC-ethanol ablations were performed to optimize the formulation (n=6). *In vivo* ablations were performed to compare the optimal EC-ethanol formulation to pure ethanol (n=6). Ablations were monitored with CT and ethanol distribution volume was quantified. Livers were explanted, sectioned and stained with NADH-diaphorase to determine the ablative extent.

Results

CT imaging of ethanol-water surrogates demonstrated the ethanol concentration-radiodensity relationship is approximately linear. A concentration of 12% EC in ethanol created the largest distribution volume, more than 8-fold that of pure ethanol, *ex vivo*. *In vivo*, 12% EC-ethanol was superior to pure ethanol, yielding a distribution volume 3 times greater and an ablation zone 6 times greater than pure ethanol.

Conclusions

EC-ethanol, a novel gel formulation injectable ablative injectate, safely increases distribution and necrosis compared to pure ethanol.

Introduction

Interventional radiology has the potential to provide care to a massive portion of the global population that does not have access to treatment for liver cancer, now the fourth leading cause of cancer-related mortality globally as of 2018 [1]. Low- and middle-income countries (LMICs) will account for 70% of cancer mortality by 2040 [2] while receiving only 5% of global cancer resources [3]. Nine out of ten people in LMICs do not have access to basic surgical care [4], transplantation rates are a tenth of those in high-income countries (HICs) [5], and access to chemotherapy is often unreliable due to cost and insufficient testing infrastructure to direct treatment regimens [6].

Thermal ablation is established as standard of care curative treatment for hepatocellular carcinoma (HCC) in the Barcelona Clinic Liver Cancer staging criteria [7]. Compared to surgery it is less expensive [8],

less invasive [9], faster [10] and requires shorter hospital stays [11]. Ablation is well-tolerated and has gained widespread acceptance [12] for treatment of primary tumors in the liver, kidney, and lung [13], precancerous lesions on the surface of the cervix [14], metastases [15], and chronic pain [16]. However, thermal ablation has a high barrier for entry to LMICs due to cost and the need for reliable electrical power requirements.

Ethanol ablation is a low cost and easy to use approach, which has been historically used to treat inoperable HCCs. Further, as a non-thermal modality, ethanol outperforms thermal ablation next to structures such as bowel, intestine, or gallbladder [17], especially in a setting where there is no computed tomography (CT) access to allow reliable deep-field hydro-dissection. However, a caveat of using ethanol is leakage into neighboring tissue, which has resulted in unpredictable ablations, need for retreatment and off-target toxicity. For ethanol ablation to be an effective alternative to thermal ablation, the localization of this agent within the target tissue needs to be addressed [18].

Ethanol mixed with a polymer, ethyl cellulose (EC), has been used clinically to treat venous malformations [19] and herniated discs [20] with minimal toxicity. The EC-ethanol mixture is a liquid. Upon injection into tissue and exposure to water, it undergoes a phase change into a cotton-like gel. Sequestration of the ethanol within the gel prevents it from leaking unpredictably from the injection site. Prior work has demonstrated that EC-ethanol shrinks tumors *in vivo* and increases survival; a single infusion of EC-ethanol in a hamster model of oral squamous cell carcinoma led to regression of 7/7 tumors versus 0/5 following treatment with pure ethanol [21]. Further work demonstrated in *ex vivo* swine liver and tissue-mimicking surrogates that infusion of EC-ethanol using controlled deliver parameters (e.g., infusion rate and volume) localizes the injected ethanol in a prescribed volume of tissue with minimal leakage [22].

The goal of this study was to establish the intra-hepatic imaging characteristics of EC-ethanol, the concentration of EC in ethanol that resulted in the largest distribution volume and lowest aspect ratio (to assess radial symmetry of the distribution volume), and the radiologic-pathologic correlation of the ablative capability of this formulation in a rat liver model. We created a quantitative approach to establish the ethanol distribution, aspect ratio and concentration in CT images of the liver, post-injection. Using this methodology, we demonstrated that a concentration of 12% EC in ethanol creates the largest distribution volume and the lowest aspect ratio compared to that of 0, 6, 8, 10 or 15% EC-ethanol in *ex vivo* liver tissue. Further, 12% EC-ethanol resulted in an 8-fold and 3-fold increase in volume in *ex vivo* and *in vivo* livers, respectively, compared to that of pure ethanol. Finally, radiological-pathologic correlation studies showed that 12% EC-ethanol yielded an ablation zone 6-fold greater than pure ethanol.

Methods

a. CT imaging acquisition and segmentation

All CT images acquired were full rotation (360°) with 180 projections at a 50 ms settlement time, medium magnification (pixel size, 78.81 μm), and a field of view of 8.07 \times 16.11 cm, in a 512 \times 512 matrix. Images were acquired at 80 kV, 500 μA with 300 ms exposure time. For *in vivo* images, a preset beam-

hardening correction was applied. Images were acquired of ethanol-water vials and *ex vivo* and *in vivo* rat livers. Images were processed in 3D Slicer [56].

The average radiodensity of *in vitro* ethanol-water samples was computed by segmenting a cylinder within each vial. *Ex vivo* liver images were segmented by selecting the tissue surrounding the injected ethanol distribution without including surrounding buffer. Ethanol was segmented by interpolating between circles of 5–15 mm on each side of the injected ethanol. Overlapping circles were used when necessary. *In vivo* images were segmented by selecting the tissue surrounding the injected ethanol without including surrounding tissues (intestines, stomach, or lungs). The same method used for *ex vivo* images was used to segment the *in vivo* liver and ethanol distributions. Sample pre- and post-ablation segmentation volumes were similar.

b. Determination of ethanol concentration and quantitation of error from radiodensity measurements of ethanol vials

Solution	Concentrations Tested (%)
Ethanol-water	0, 25, 50, 75, 100 (n=20)
Iohexol-ethanol	0, 2, 5, 7.5, 10 (n=3)
Ethyl cellulose-ethanol	0, 3, 6, 8, 10, 12, 15 (n=3)
Fluorescein-ethanol	0, 0.25, 1, 2.5 (n=3)

Solutions were imaged with CT and segmentation was performed as described above. Radiodensity data was converted to ethanol concentration with a linear two-point calibration equation (**equation (1)**), which corresponded to a five-point calibration. Calibration was performed at the beginning of each imaging session. For *in vitro* experiments, vials of pure ethanol and water were imaged to serve as 100% and 0% ethanol standards, respectively. In the liver studies, the 0% ethanol standard was the average radiodensity of the pre-ablation liver, since tissue has slightly higher radiodensity than water. The radiodensity difference of the 0% and 100% standards represents the radiodensity range for all possible ethanol concentrations (denominator). The radiodensity difference between the sample and the 0% ethanol standard was calculated (numerator) and divided by the radiodensity range for all possible ethanol concentrations (denominator) to determine the sample ethanol concentration. **Equation (1)** assumes a linear relationship between ethanol concentration and radiodensity, and that sample thickness does not affect measurement accuracy. **Supplementary Fig. S2** illustrates application of this equation.

$$\text{Ethanol concentration} = \frac{\text{Radiodensity}_{\text{sample}} - \text{Radiodensity}_{0\% \text{ ethanol standard}}}{\text{Radiodensity}_{100\% \text{ ethanol standard}} - \text{Radiodensity}_{0\% \text{ ethanol standard}}} \times 100\% \quad \text{Equation (1)}$$

c. Description of animal work

All animal studies were approved by the Duke University Institutional Animal Care and Use Committee and performed in accordance with guidelines and regulations (Protocol Number A160-18-07). Male Fischer CDF rats (Charles River Laboratories) were used for *ex vivo* (n=36 lobes, n=10 rats) and *in vivo* studies (n=12 rats). Male rats were used since anatomical imaging and ethanol concentrations should be insensitive to gender and liver cancer incidence is higher in males than females [1]. Rats had ad libitum food and water access and regular 12-hour light/dark cycles.

d. *Ex vivo* rat liver studies

Rats were euthanized via isoflurane overdose and bilateral thoracotomy. The liver was immediately excised and stored in Krebs-Ringer bicarbonate buffer (Sigma Aldrich, K4002) on ice until injection (within 1–2 h). Individual lobes were placed in a small plastic container (height, 62.6 mm; diameter, 41.9 mm) for injection. A 27-gauge needle was lowered to the approximate center of the lobe using a holder to prevent lateral motion. Fluid was infused from a 3-mL syringe (BD Medical, Columbus, NE) through 10 cm of rubber tubing (1/4" inner diameter, McMaster-Carr, Douglasville, GA) using a syringe pump (NE-1000, New Era, Farmingdale, NY) at a flow rate of 10 mL/h. Prior work demonstrated that 10mL/hr is optimal compared to 0.1, 1, and 100mL/hr[21] 100 μ L of fluid was infused based on infusion volumes previously optimized to reduce leakage [22] and the rat liver size. The needle was removed 3 minutes after infusion to allow fluid to dissipate. Non-contrast CT images of the samples were acquired pre- and post-injection with EC-ethanol (0%, 6%, 8%, 10%, 12% or 15%).

e. *In vivo* rat liver studies

Pre-ablation non-contrast CT images of the rat abdomen were acquired. Rats were maintained with 1.5% isoflurane at 2 L/min during the procedure and a heating pad maintained body temperature. Buprenorphine Sustained-Release (1 mg/kg) was administered subcutaneously as an analgesic. The abdomen was depilated and disinfected three times with 10% povidone-iodine followed by 70% ethanol. A laparotomy was performed by creating an incision with a sterile scalpel through the skin and abdominal wall to expose the left lateral lobe of the liver. A sterile cotton-tipped applicator was used to expose the center of the left lateral liver lobe. Injections were performed as described above for the *ex vivo* studies. The needle was slowly retracted and a cotton-tipped applicator was used to stop any visible bleeding. The abdominal wall was closed with Reli monofilament sutures (VWR, 89219-212). 1-2 drops of 0.25% bupivacaine were applied along the incision as a local anesthetic. The skin was closed with Coated VICRYLÒ (polyglactin 910) sutures (VWR, 95057-014). Post-injection non-contrast CT images of the liver were acquired.

Animals were monitored post-ablation every 6-8 h for 24 h for: mobility impairment; inflammation/edema; bleeding; respiratory distress; loss in body weight; licking, biting, scratching or shaking of procedure site; hair coat changes; posture; and lethality. Rats were euthanized by isoflurane overdose 24 h after ablation and the liver was immediately excised. The left lateral lobe was cut into three 2x2 cm samples. Samples were placed into Peel-A-WayÒ disposable embedding molds (Polysciences Inc., 18646A-1, Warrington PA), labeled, and covered in optimum cutting temperature (OCT) gel (Sakura Finetek, Torrance, CA). The

molds were placed in a metal container of 2-methylbutane (Sigma, 277258) and frozen using liquid nitrogen. Samples were stored in a -80°C freezer.

f. Ethanol distribution volume and radial symmetry of *ex vivo* and *in vivo* liver tissues

Maximum intensity projection images were produced from the 3D segmentation by projecting the voxel with the highest estimated ethanol concentration onto a 2D image from top- and side-view perspectives. An 20% ethanol concentration threshold was used because a 10-min exposure of 20% ethanol is cytotoxic [25] and imaging were acquired 10-20 min after injection. **Supplementary Fig. S3** illustrates that this threshold excludes regions of naturally low radiodensity in untreated tissue from analysis. Ethanol distribution volume was calculated by converting total number of voxels with ethanol concentration 20% to volume. The degree of asymmetry of the ethanol distribution was quantified by the aspect ratio, as in **equation (2)**—the radius of gyration over the effective radius—for all voxels with estimated ethanol concentration 20%.

$$\text{Aspect ratio} = \frac{\text{Radius of gyration}}{\text{Effective radius}} = \frac{\sum \text{Distance from centroid} / \text{number of pixels}}{\sqrt[3]{3 * \text{Volume} / 4\pi}} \quad \text{Equation (2)}$$

g. Pathologic evaluation of ablative extent

To assess the extent of necrosis, two 7- μm sections were cut serially every 1 mm from frozen samples at -15°C with a cryostat microtome (Microm HM 560, Thermo Fisher Scientific, Waltham, MA). Serial sections were adhered to positively-charged, uncoated glass slides (Thermo Fisher Scientific, 6776214). One slide from each pair was stained with reduced nicotinamide adenine dinucleotide (NADH)-diaphorase, a viability stain which distinguishes viable cells (blue) from necrotic cells (unstained). The slides were covered in Tris buffer (0.05 M, pH 7.6) with 8 mg / 5 mL NADH (Sigma, N8129) and 10 mg / 5 mL nitro blue tetrazolium (Sigma, N6876) and incubated for 15 min at 37°C. Slides were then washed three times with deionized water followed by three exchanges in 30%, 60%, and 90% acetone. The slide was covered in 90% acetone until a purple cloud appeared in the solution. Slides were washed three times with deionized water and allowed to dry. Coverslips (Thermo Fisher Scientific, 12540C) were applied with aqueous mounting medium prepared by mixing 21 mL of deionized water, 4 g of store-grade unflavored gelatin, 25 mL of glycerol (Sigma, G2025), and 0.5 mL of phenol (Sigma, P9346) at low heat.

Sectioning was performed beginning with the sample from the distal end of the liver lobe. The second sample was sectioned and stained using the same procedure. If no necrosis was observed in any sections in the second sample, the third sample was not sectioned or stained; otherwise, the third section was sectioned and stained using the same procedure.

h. Image analysis of pathology specimens from *in vivo* liver tissues

Slides were digitally scanned at 10x magnification with a Zeiss Axio Imager Z2 upright microscope. The region of interest (ROI), or necrotic area, was determined using a custom MATLAB program. Images were cropped to remove portions that did not contain tissue. First the tissue was segmented by applying an entropy filter to the blue channel of the images and binarizing the result using a user-defined threshold. Small regions (<15,000 connected pixels) were deleted to remove noise. The edges of the regions were eroded using a flat structuring element with a 15 pixel neighborhood, holes in the regions were filled, and the edges of the regions were dilated using the same structuring element. The boundaries of the tissue sample were detected and the area was quantified using the MATLAB function 'regionprops'. A mask generated from the binary image was used to remove background pixels from the original image.

The resultant image was then used to segment the necrotic area. The blue channel was binarized with a user-defined threshold, and small regions <5,000 pixels were removed. All ROIs except for the five largest were deleted from the image. Regions such as large vasculature which may be detected under the same threshold used for necrosis were manually selected for removal. The boundaries of the necrotic regions were detected and the MATLAB function 'regionprops' was used to quantify area. **Supplementary Fig. S4** shows representative images each step. Necrotic volume was calculated by multiplying necrotic area by the sectioning step size (1 mm) and taking the sum for all samples for each animal. All images were processed by one user. Adjacent H&E slides were used for confirmation. The semi-automated MATLAB algorithm was compared to gold standard manual segmentation using ImageJ software. Digital images from the sections of two samples (1 per group) were manually segmented. For the 13 images assessed, the MATLAB algorithm estimated an average of 0.0465 cm² more necrotic area than manual segmentation, with an average absolute scalar difference of 0.0049 cm². **Supplementary Fig. S5** shows the comparative analysis of the necrotic areas determined manually and using the MATLAB algorithm.

Results

a. CT radiodensity values show a linear relationship with ethanol concentration

To investigate whether the presence of EC affects the ethanol concentration estimation, EC was dissolved in ethanol at different concentrations and the mixtures were imaged by CT. **Figure 1c** demonstrates that radiodensity was not impacted by the presence of EC, verifying that CT imaging assesses the impact of EC on the spread of injected ethanol and not the presence of EC itself. **Supplementary Fig. S1** illustrates the effect of fluorescein and iohexol on radiodensity when dissolved in ethanol. Radiodensity was not impacted by the presence of fluorescein, but increased for iohexol concentrations of 5% or greater, at which iohexol is insoluble. Iohexol was not used in the *ex vivo* or *in vivo* experiments. Fluorescein was included in the *ex vivo* samples.

b. 12% EC achieves the largest ethanol distribution volume and lowest aspect ratio of injected ethanol in *ex vivo* liver

Clinical use of ethanol ablation has been limited due to leakage of ethanol from the injection site, reducing tumor coverage and causing adverse off-target effects [24]. Ethanol ablation can be improved by localizing the ethanol distribution within a defined region by using gel-forming polymers. We used an *ex vivo* rat liver model to quantify ethanol localization following injection of EC-ethanol, defined by the volume and aspect ratio of the ethanol distribution within the tissue. Although previous work has demonstrated that incorporation of EC reduces leakage and improves efficacy of ethanol ablation [21], the EC concentration which achieves a predictable, uniform distribution and reduces off-target leakage is unknown. EC-ethanol solutions containing over 15% EC have high viscosity and are difficult to inject with standard syringes and tubing; therefore, we capped the EC concentration at 15%. In each *ex vivo* rat liver sample, 100 μL of EC-ethanol [22] at 0%, 6%, 8%, 10%, 12%, and 15% EC ($n=6$ per group) was injected at a rate of 10 mL/h. Pre- and post-ablation CT images were acquired.

Figure 2a shows representative transverse (top row) and frontal (bottom row) cross-sectional post-ablation CT images of containers of tissue submerged in buffer. Tissue appears brighter (higher radiodensity) than buffer; dark pixels (lower radiodensity) within the tissue correspond to injected ethanol. Maximum concentration projections, shown in **Fig. 2b**, display the 3D ethanol distributions maximally projected onto a 2D plane. Each maximum concentration projection was created by projecting the voxel with the highest ethanol concentration onto a 2D image in either the transverse (top row) or frontal (bottom row) perspective. Since the pre-ablation liver has naturally occurring regions of low radiodensity that appear similar to dilute ethanol, a minimum threshold of 20% ethanol ensures that these regions are not included in our analysis, as illustrated in **Supplementary Fig. S6a**. As in the images in **Fig. 2a**, the darker pixels of the maximum concentration projections shown in **Fig. 2b** correspond to higher ethanol concentrations. Concentrations of 20% ethanol or higher are cytotoxic at the imaging time post-ablation [25]; therefore, the volume of ethanol within the tissue at an estimated concentration of 20% or greater was our primary metric for optimization. 3D segmentations, shown in **Fig. 2c** with the volume of each segmentation listed below, show the injected ethanol distributions (green) within the liver (pink). The images shown in **Fig. 2** demonstrate that EC-ethanol ablation leads to regions of highly concentrated ethanol surrounded by regions of less concentrated ethanol within the tissue.

Image data was converted from units of radiodensity to ethanol concentration with a linear two-point calibration equation (**equation(1)**) using pre-injection tissue radiodensity and the radiodensity of pure ethanol as the standard for 0% and 100% ethanol, respectively. Cumulative volume histograms (i.e. the average ethanol volume above a given concentration, $n=6$), shown in **Fig. 3a**, illustrate that 12% EC in ethanol results in the largest distribution of $\geq 20\%$ ethanol. **Figure 3b** shows the average pre- and post-ablation distribution volumes with estimated ethanol concentrations $\geq 20\%$. Pure ethanol had the lowest distribution volume, $17.1 \pm 12.9 \mu\text{L}$. The incorporation of 12% EC yielded the greatest distribution volume ($137.7 \pm 64.3 \mu\text{L}$), significantly greater than ethanol alone ($p < 0.01$), an >8 -fold improvement. Further this distribution is closest to the actual injection volume of 100 μL . 12% EC-ethanol also yielded significantly greater distribution volumes than 6% ($42.9 \pm 24.8 \mu\text{L}$, $p < 0.01$), 10% ($63.5 \pm 30.2 \mu\text{L}$, $p < 0.05$), and 15% EC-ethanol ($67.9 \pm 37.0 \mu\text{L}$, $p < 0.05$).

The incorporation of EC not only increased ethanol accumulation within the tissue, but also led to a more spherical ethanol distribution, quantified using the aspect ratio, as shown in equation (2), which is the ratio of the average distance of each point in the distribution to the centroid (radius of gyration) to the radius of a spherical distribution of equivalent volume (effective radius). A sphere has the lowest possible aspect ratio (1), whereas more asymmetric distributions have greater aspect ratios. Spherical ablation indicates minimal leakage and allows clinicians to plan the needle insertion location for lesions of any size; distributions with irregular shapes complicate ablation planning. **Figure 3c** shows the average aspect ratio for each injection group. Injections of 12% EC-ethanol produced the lowest aspect ratio (1.09 ± 0.12), significantly more spherical than injections of pure ethanol (3.27 ± 2.83 , $p < 0.05$).

c. 12% EC achieves a more localized injection distribution and greater volume of necrosis compared to conventional ethanol ablation in an *in vivo* liver model

12% EC in ethanol is most effective in maximizing the distribution volume and achieving an aspect ratio close to unity in an *ex vivo* rat liver model. Next, we investigated whether 12% EC induced a larger zone of necrosis than pure ethanol in an *in vivo* rat liver model. Ablations were performed by injecting 100 μL of 12% EC-ethanol or pure ethanol ($n=6$) at a rate of 10 mL/h into the left lateral liver lobe *in vivo*. CT images of the liver were acquired 10 minutes pre- and post-ablation. Tissue was excised 24 h post-ablation to determine the extent of ablation via pathologic analysis. **Figures 4a** and **4b** depict frontal plane cross-sectional CT images of pure ethanol and 12% EC-ethanol ablations, respectively. Ethanol appears as a black area and is indicated by a black arrow within the liver. **Figures 4c** and **4d** show maximum concentration projections, compiled using the same method as in **Fig. 2b**, for the frontal (top row) and transverse (bottom row) views for pure ethanol and 12% EC-ethanol ablations. For pure ethanol, the areas containing the highest estimated ethanol concentrations appear as multiple black foci, whereas the maximum concentration projections for 12% EC-ethanol depict a large continuous fluid distribution consisting mainly of concentrated ethanol. **Figs. 4e** and **4f** show segmented images from frontal and transverse views of a pure ethanol and a 12% EC-ethanol ablation, with the green region depicting the injected ethanol distribution and the pink region showing soft tissue. The pure ethanol distribution consists of multiple small, non-contiguous distributions. In contrast to pure ethanol, the segmentation for 12% EC-ethanol shows a single, contiguous ethanol distribution.

To determine the extent of ablation, tissue was excised 24 h after injection, cryopreserved, sectioned, and stained with NADH-diaphorase. NADH-diaphorase stains viable tissue blue and non-viable tissue gray. Representative sections of tissue stained with NADH-diaphorase after ablation with pure ethanol and 12% EC-ethanol are shown in **Fig. 4g** and **4h**, respectively. The image shows a necrotic area, outlined in red, surrounded by viable liver tissue. To approximate the volume of induced necrosis, the area of necrosis on each slide was quantified by a process described in **Supplementary Fig. S4** and verified with manual segmentation (**Supplementary Fig. S5**). To quantify volume, the necrotic area from each slide was multiplied by the sectioning step-size and summed. After ablation, animals did not exhibit mobility

impairment, inflammation/edema, bleeding, respiratory distress, loss in body weight, hair coat changes, posture changes or lethality.

The average cumulative volume histograms for pure ethanol and 12% EC-ethanol, shown in **Fig. 5a**, demonstrate that 12% EC-ethanol yields a larger distribution volume of $\geq 20\%$ ethanol than pure ethanol. This analysis indicates that some tissue has an estimated ethanol concentration greater than 100%, possibly due to the inclusion of air bubbles within the tissue that may have entered the tissue during the open surgical procedure. The magnitude of this artifact in comparison to pure ethanol and the *ex vivo* injections is detailed in **Supplementary Fig. S5**. To account for the presence of air bubbles in our analysis, voxels with an estimated ethanol concentration $>120\%$ were excluded in quantification of the ethanol distribution. **Figure 5b** illustrates that the aspect ratio for 12% EC-ethanol was also more favorable than that of pure ethanol (1.39 ± 0.51 vs. 1.58 ± 0.66 , NS) indicating a more spherical ethanol distribution.

Figure 5c shows *in vivo* ethanol distribution volumes and necrotic volumes for the ethanol and 12% EC-ethanol groups. Confirming our *ex vivo* results, an EC concentration of 12% led to a significantly greater distribution volume than pure ethanol ($320.9 \pm 291.9 \mu\text{L}$ vs. $109.6 \pm 56.0 \mu\text{L}$, $p < 0.05$), a near 3-fold improvement. The incorporation of 12% EC led to a >6 -fold increase in necrotic volume versus pure ethanol ($326.5 \pm 436.4 \mu\text{L}$ vs. $50.9 \pm 67.2 \mu\text{L}$, $p < 0.05$). For each sample, the ratio of necrotic volume to ethanol distribution volume determined by CT was calculated and is shown in **Fig. 5d**. The average ratio of necrotic volume to ethanol distribution volume is greater for 12% EC-ethanol than for pure ethanol (0.98 ± 0.65 vs. 0.51 ± 0.48 , NS).

Discussion

Ethanol ablation induces coagulative necrosis by denaturing cellular proteins [26] and dehydrating the cytoplasm [27], and causes ischemia by damaging vascular endothelial cells [28]. For ethanol ablation to be effective, the target tissue must reach a cytotoxic concentration of 20% ethanol or greater [25]. Drastically reducing the infusion rate can prevent rupture and improve intratumoral accumulation [29], but is too time-consuming to implement for treatment of large tumors. Intratumoral delivery within a clinically-feasible duration requires an infusion rate that pressurizes tissue to the point of rupture forming low-resistance paths (i.e., cracks) allowing fluid to leak away from the injection site [30]. Incorporation of ethyl cellulose (EC), an ethanol-soluble, water-insoluble polymer, induces formation of a fibrous gel phase upon exposure to tissue, and improves tumor coverage as the gel sequesters ethanol at the target site. *In situ* gelation is appealing as a means to maintain a high ethanol concentration within a region of interest at a clinically reasonable infusion rate without the formation of cracks.

CT imaging was utilized because it is rapid and non-destructive, which is necessary due to the difference in timescales of ethanol flow (minutes) and its ablative effect (days). Ultrasound imaging has been used previously to monitor the spread of injected ethanol [31]; however, 3D reconstruction of 2D ultrasound images is difficult. Both magnetic resonance imaging [32] and CT [23] allow 3D visualization of injected ethanol, with CT imaging lending itself to easier quantification arising from diminished soft tissue

contrast and imaging field gradients as noise sources [33]. CT imaging has previously been demonstrated to exhibit strong predictive ability in mapping drug dose distribution following trans-arterial chemoembolization [34]. Utilizing ethanol-water mixtures as *in vitro* tissue surrogates in this study, ethanol demonstrated a linear relationship between radiodensity and ethanol concentration [23] to segment a cytotoxic delivery threshold as the slight non-linearity introduces an error of 7.7%. This non-linearity reflects the documented non-linearity in the relationship between physical density and ethanol concentration [35], as physical density is proportional to electron density, and therefore radiodensity [36]. The measurement error arising from quantum noise (i.e., random noise) was 7.6%. Both errors are significantly smaller than the threshold of 20% ethanol concentration.

Ethanol concentration and distribution in tissue were imaged by CT and quantified using the natural contrast between ethanol and water [23]. Treated and non-treated regions were segmented using a 20% ethanol concentration threshold. A formulation of 12% EC-ethanol caused negligible leakage and the largest and most spherical ethanol distribution volume in *ex vivo* rat liver, eight-fold greater than pure ethanol. This formulation also improved distribution volume by three-fold and increased the zone of pathologic necrosis by six-fold compared to pure ethanol in *in vivo* rat liver. Compared to pure ethanol, 12%EC-ethanol increases ethanol distribution volume more in the *ex vivo* studies than the *in vivo* studies and the difference between the aspect ratios is significant for the *ex vivo* studies and not the *in vivo* studies. This disparity likely occurs because in the *ex vivo* samples the vasculature is collapsed and the tissue has been removed from the body and submerged in buffer. Therefore, the collapsed vasculature leads to a tissue-buffer barrier where the buffer provides little or no impedance to ethanol flow. *In vivo* the vasculature is not collapsed and contains flowing blood. Injections performed *in vivo* can be considered a closed system. Both pure ethanol and 12% EC-ethanol achieve greater distributions volumes *in vivo* compared to the volumes achieved *ex vivo*, suggesting that leakage out of the tissue into the buffer space decreases the observed volume. The comparative fold- increase is smaller *in vivo* since the closed system prevents leakage out of the tissue, which is more significant for pure ethanol, as it is less viscous. Further, EC-ethanol volume observed on CT corresponded to necrosis observed in histology, demonstrating reliable radiologic-pathologic correlation with CT as a non-invasive pathology surrogate. These studies characterized CT imaging for use in future optimization of EC-ethanol ablation protocols and established a methodology that can be implemented in the development of intra-tumoral delivery of other therapeutic agents.

The current study demonstrates suitability of CT imaging in evaluating delivery in the context of optimizing the ablation protocols and the near equivalence of the EC-ethanol distribution volume to the necrotic volume validates the relevance of imaging. The equivalency of these the two volumes for EC-ethanol indicates that the distribution volumes as determined by ethanol concentration extraction and concentration-based thresholding is an accurate representation of the resultant ablative effect. In contrast, the distributions visualized on CT for pure ethanol do not show equivalency to the resultant necrotic volumes, offering a potential explanation for why conventional ethanol ablation requires multiple treatment sessions or injections [18, 37-39]. Although histopathology is the gold standard for demonstrating therapeutic effect, its use in the assessment of intra-tumoral drug delivery is challenging

because tissue must be sectioned, and treated tissue often spans multiple sections. Aligning individual specimens to reconstruct the *in vivo* configuration is not possible because tissue preparation requires sectioning into multiple tissue blocks that deform during preparation. CT imaging is a quicker, non-destructive, and simpler method than histopathology to assess efficacy of ablation.

In addition to the improvement in delivery as quantified by the ethanol distribution volume achieved with 12% EC, the comparative ratios of ethanol distribution-to-necrotic volume is indicative of the ethanol release profile. The ratio of the necrotic volume to ethanol distribution volume was greater for 12% EC-ethanol than for pure ethanol. Although not statistically significant, this finding potentially arises from the prolonged exposure time associated with gel formation in concordance with delayed vascular clearance achieved by EC in the ablation of venous malformations [19]. Longitudinal imaging of the ethanol distribution is necessary to better understand this effect and confirmation of delayed clearance would make combination of EC-ethanol with other therapeutic agents synergistic as ethanol may extend the therapeutic effect.

With growing interest in injectable stimuli-response polymers [40] to locally deliver chemo- and immunotherapy [41, 42], assessment of intratumoral delivery is crucial to implementation. The methodology described here can be implemented to assess delivery of other therapeutic agents using the desired concentration to determine the thresholding strategy and including an exogenous contrast agent if necessary. We considered adding a contrast agent to the injection solution to improve contrast between the injectate and tissue. Unfortunately, there are few radio-contrast agents that are ethanol-soluble. We tested iohexol, a radiopaque iodine-based radio-contrast agent. At 5% iohexol, the solubility limit in ethanol, the contrast to tissue was comparable to that of ethanol alone, and at high concentrations iohexol can cause streaking artifacts in CT images. Additionally, iohexol has a molar mass that is 20x greater than that of ethanol; therefore, its transport in tissue may differ from that of ethanol. Overall, we found that ethanol alone has sufficient contrast with surrounding tissue, particularly when excluding regions with <20% ethanol.

We recognize several limitations of our study. First, we used a two-point calibration curve to calculate estimated ethanol concentration in *ex vivo* and *in vivo* experiments because creation of tissue-ethanol mixtures at known concentrations is not feasible. Although including intermediate points would increase accuracy, the error in estimated ethanol concentration is small compared to the volumes measured in the tissue samples and should not affect the conclusions drawn in our study. A further limitation is that our study was performed in healthy rat liver tissue, which is more homogenous than cancerous lesions. We plan to assess the impact of tissue heterogeneity on the ethanol distribution in cancerous lesions in future studies. Another limitation was the small size of the rat liver. Both pure ethanol and 12% EC-ethanol showed a relatively large variance in the volume of ethanol accumulated in the tissue; however, it was difficult to ensure that the needle was placed in the center of the lobe and not near a large vessel, which would have artificially affected the distribution volume. Although not possible due to the small size of the animals in this study, clinically, ethanol ablations are often guided by ultrasound [26, 39, 43-48] or CT [23, 49] to insert the needle to a precise location, mitigating issues associated with needle placement.

For future large animal studies, the use of ultrasound or CT to guide needle placement and avoid large vasculature would likely reduce the variance in accumulated ethanol volume.

This optimized form of ethanol ablation is poised for immediate application in LMICs and HICs alike. The improved delivery achieved here obviates the need for large ethanol volumes and multiple treatment sessions limiting adverse non-target effects. While thermal ablation is the first-line therapy for liver tumors [50] in HICs, it is not well-suited for tumors proximal to vital structures such as bile ducts, intestinal loops, gall bladder) or along the capsule [17] because heat is more readily transmitted between organs than liquid. As a result, ethanol ablation is often recommended for these high-risk locations [51] and EC incorporation should improve targeting. In LMICs, EC-ethanol is appealing because it eliminates the loss to follow-up, does not require multiple sessions [52] as would be required with conventional ethanol ablation and is poised to expand access as it is low-cost, minimally invasive, highly portable, and electricity independent. The growing accessibility of ultrasound [53] and its widespread history in targeting ethanol ablation [54] facilitates image-guided ablation of primary tumors or metastases in the kidney, liver, and breast tumor with either curative or palliative intent when no alternate treatment is available. Further, EC-ethanol ablation could supplement cryotherapy and thermocoagulation to treat of superficial lesions such as oral and cervical precancerous lesions without the need for hard-to-supply consumables [55]. These studies characterized CT imaging for use in future optimization of EC-ethanol ablation protocols and established a methodology that can be implemented in the development of intratumoral delivery of other therapeutic agents.

Declarations

Acknowledgments:

The authors thank the Translational PET/CT Molecular Imaging Center at Duke University, including Dr. Satish K. Chitneni and Thomas Hawk, for assistance with acquiring the CT images presented in this manuscript. The studies in this manuscript were funded by the NIH (R01CA239268, and F31CA239623), North Carolina Biotechnology Center (Biotechnology Innovation Grant: , NCBC GRANT #2018-BIG-6524), and the Core Facility Voucher Program through the Duke School of Medicine. The authors thank Dr. David F. Katz for his assistance with the Core Facility Voucher Program application.

Author contributions:

R.M., E.C., C.N., B.C., A.A.S., and N.R. designed the experiments. R.M. and E.C. carried out the experiments and analyzed the data. R.M and E.C. took the lead in writing the manuscript and preparing figures. All authors provided critical feedback and helped shape the research, analysis and manuscript.

Additional Information:

Competing Interests: The author(s) declare no competing interests.

References

1. Bray, F., et al., *Global cancer statistics 2018: GLOBOCAN estimates of incidence and mortality worldwide for 36 cancers in 185 countries*. CA Cancer J Clin, 2018. **68**(6): p. 394-424.
2. Bray, F. and I. Soerjomataram, *The Changing Global Burden of Cancer: Transitions in Human Development and Implications for Cancer Prevention and Control*, in *Cancer: Disease Control Priorities, Third Edition (Volume 3)*, H. Gelband, et al., Editors. 2015, World Bank Publications: Washington DC.
3. Farmer, P., et al., *Expansion of cancer care and control in countries of low and middle income: a call to action*. Lancet, 2010. **376**(9747): p. 1186-93.
4. Meara, J.G., et al., *Global Surgery 2030: evidence and solutions for achieving health, welfare, and economic development*. Lancet, 2015. **386**(9993): p. 569-624.
5. Organization, W.H., *Global observatory on donation and transplantation*. 2017.
6. Ruff, P., et al., *Access to Cancer Therapeutics in Low- and Middle-Income Countries*. Am Soc Clin Oncol Educ Book, 2016. **35**: p. 58-65.
7. Llovet, J.M., C. Brú, and J. Bruix, *Prognosis of hepatocellular carcinoma: the BCLC staging classification*. Semin Liver Dis, 1999. **19**(3): p. 329-38.
8. Sullivan, R., et al., *Global cancer surgery: delivering safe, affordable, and timely cancer surgery*. Lancet Oncol, 2015. **16**(11): p. 1193-224.
9. Bilchik, A.J., et al., *Radiofrequency ablation: a minimally invasive technique with multiple applications*. Cancer J Sci Am, 1999. **5**(6): p. 356-61.
10. Kanotra, S.P., M. Lateef, and O. Kirmani, *Non-surgical management of benign thyroid cysts: use of ultrasound-guided ethanol ablation*. Postgraduate Medical Journal, 2008. **84**(998): p. 639.
11. Lü, M.D., et al., *Surgical resection versus percutaneous thermal ablation for early-stage hepatocellular carcinoma: a randomized clinical trial*. Zhonghua yi xue za zhi, 2006. **86**(12): p. 801.
12. Saldanha, D.F., et al., *Current tumor ablation technologies: basic science and device review*. Semin Intervent Radiol, 2010. **27**(3): p. 247-54.
13. Ridouani, F. and G. Srimathveeravalli, *Percutaneous image-guided ablation: From techniques to treatments*. Presse Med, 2019. **48**(7-8 Pt 2): p. e219-e231.
14. Luciani, S., et al., *Effectiveness of cryotherapy treatment for cervical intraepithelial neoplasia*. Int J Gynaecol Obstet, 2008. **101**(2): p. 172-7.
15. Kurup, A.N., J.M. Morris, and M.R. Callstrom, *Ablation of Musculoskeletal Metastases*. AJR Am J Roentgenol, 2017. **209**(4): p. 713-721.
16. Sindt, J.E. and S.E. Brogan, *Interventional Treatments of Cancer Pain*. Anesthesiol Clin, 2016. **34**(2): p. 317-39.
17. Kwon, J.H., *Is percutaneous ethanol injection therapy still effective for hepatocellular carcinoma in the era of radiofrequency ablation?* Gut Liver, 2010. **4 Suppl 1**: p. S105-12.

18. Shiina, S., et al., *Percutaneous ethanol injection therapy for hepatocellular carcinoma. A histopathologic study.* Cancer, 1991. **68**(7): p. 1524-30.
19. Sannier, K., et al., *A new sclerosing agent in the treatment of venous malformations. Study on 23 cases.* Interv Neuroradiol, 2004. **10**(2): p. 113-27.
20. Volpentesta, G., et al., *Lumbar percutaneous intradiscal injection of radiopaque gelified ethanol ("Discogel") in patients with low back and radicular pain.* J Pain Relief, 2014. **3**(145): p. 2167-0846.
21. Morhard, R., et al., *Development of enhanced ethanol ablation as an alternative to surgery in treatment of superficial solid tumors.* Sci Rep, 2017. **7**(1): p. 8750.
22. Morhard, R., et al., *Understanding factors governing distribution volume of ethyl cellulose-ethanol to optimize ablative therapy in the liver.* 2019: Submitted to IEEE Transactions on Biomedical Engineering.
23. Alexander, D.G., et al., *Estimation of volumes of distribution and intratumoral ethanol concentrations by computed tomography scanning after percutaneous ethanol injection.* Acad Radiol, 1996. **3**(1): p. 49-56.
24. Koda, M., et al., *Hepatic vascular and bile duct injury after ethanol injection therapy for hepatocellular carcinoma.* Gastrointest Radiol, 1992. **17**(2): p. 167-9.
25. Tapani, E., et al., *Toxicity of ethanol in low concentrations. Experimental evaluation in cell culture.* Acta Radiol, 1996. **37**(6): p. 923-6.
26. Ishii, H., et al., *Local recurrence of hepatocellular carcinoma after percutaneous ethanol injection.* Cancer, 1996. **77**(9): p. 1792-6.
27. Ryu, M., et al., *Therapeutic results of resection, transcatheter arterial embolization and percutaneous transhepatic ethanol injection in 3225 patients with hepatocellular carcinoma: a retrospective multicenter study.* Jpn J Clin Oncol, 1997. **27**(4): p. 251-7.
28. Kawano, M., *An experimental study of percutaneous absolute ethanol injection therapy for small hepatocellular carcinoma: effects of absolute ethanol on the healthy canine liver.* Gastroenterol Jpn, 1989. **24**(6): p. 663-9.
29. Boucher, Y., et al., *Intratumoral infusion of fluid: estimation of hydraulic conductivity and implications for the delivery of therapeutic agents.* Br J Cancer, 1998. **78**(11): p. 1442-8.
30. Netti, P., F. Travascio, and R. Jain, *Coupled macromolecular transport and gel mechanics: poroviscoelastic approach.* AIChE Journal, 2003. **49**(6): p. 1580-1596.
31. Sugiura N, T.K., Ohto M, Okuda K, Hirooka N, *Percutaneous intratumoral injection of ethanol under ultrasound imaging for treatment of small hepatocellular carcinoma.* Acta Hepatol Jpn, 1983. **21**(920).
32. Lu, D.S., et al., *MR-guided percutaneous ethanol ablation of liver tissue in a .2-T open MR system: preliminary study in porcine model.* J Magn Reson Imaging, 1997. **7**(2): p. 303-8.
33. Krupa, K. and M. Bekiesinska-Figatowska, *Artifacts in magnetic resonance imaging.* Pol J Radiol, 2015. **80**: p. 93-106.

34. Mikhail, A.S., et al., *Mapping Drug Dose Distribution on CT Images Following Transarterial Chemoembolization with Radiopaque Drug-Eluting Beads in a Rabbit Tumor Model*. *Radiology*, 2018. **289**(2): p. 396-404.
35. Pečar, D. and V. Doleček, *Volumetric properties of ethanol–water mixtures under high temperatures and pressures*. *Fluid phase equilibria*, 2005. **230**(1-2): p. 36-44.
36. DenOtter, T.D. and J. Schubert, *Hounsfield Unit*, in *StatPearls*. 2020: Treasure Island (FL).
37. Livraghi, T., et al., *Hepatocellular carcinoma and cirrhosis in 746 patients: long-term results of percutaneous ethanol injection*. *Radiology*, 1995. **197**(1): p. 101-8.
38. Shiina, S., et al., *Percutaneous ethanol injection therapy for hepatocellular carcinoma: results in 146 patients*. *AJR Am J Roentgenol*, 1993. **160**(5): p. 1023-8.
39. Livraghi, T., et al., *Percutaneous ethanol injection in the treatment of hepatocellular carcinoma in cirrhosis. A study on 207 patients*. *Cancer*, 1992. **69**(4): p. 925-9.
40. Fakhari, A. and J. Anand Subramony, *Engineered in-situ depot-forming hydrogels for intratumoral drug delivery*. *J Control Release*, 2015. **220**(Pt A): p. 465-475.
41. Baird, J.R., et al., *Intratumoral injection of STING ligand promotes abscopal effect*. *Journal for ImmunoTherapy of Cancer*, 2014. **2**(3): p. 1-1.
42. Weinberg, B.D., et al., *Antitumor efficacy and local distribution of doxorubicin via intratumoral delivery from polymer millirods*. *J Biomed Mater Res A*, 2007. **81**(1): p. 161-70.
43. Lencioni, R., et al., *Long-term results of percutaneous ethanol injection therapy for hepatocellular carcinoma in cirrhosis: a European experience*. *Eur Radiol*, 1997. **7**(4): p. 514-9.
44. Vilana, R., et al., *Tumor size determines the efficacy of percutaneous ethanol injection for the treatment of small hepatocellular carcinoma*. *Hepatology*, 1992. **16**(2): p. 353-7.
45. Lencioni, R., et al., *Single-session percutaneous ethanol ablation of early-stage hepatocellular carcinoma with a multipronged injection needle: results of a pilot clinical study*. *J Vasc Interv Radiol*, 2010. **21**(10): p. 1533-8.
46. Tapani, E., T. Vehmas, and P. Voutilainen, *Effect of injection speed on the spread of ethanol during experimental liver ethanol injections*. *Acad Radiol*, 1996. **3**(12): p. 1025-9.
47. Shiina, S., et al., *Percutaneous ethanol injection in the treatment of liver neoplasms*. *AJR Am J Roentgenol*, 1987. **149**(5): p. 949-52.
48. Giorgio, A., et al., *Percutaneous radiofrequency ablation of hepatocellular carcinoma compared to percutaneous ethanol injection in treatment of cirrhotic patients: an Italian randomized controlled trial*. *Anticancer Res*, 2011. **31**(6): p. 2291-5.
49. Hamuro, M., et al., *Percutaneous ethanol injection under CT fluoroscopy for hypervascular hepatocellular carcinoma following transcatheter arterial embolization*. *Hepatogastroenterology*, 2002. **49**(45): p. 752-7.
50. Gosalia, A.J., P. Martin, and P.D. Jones, *Advances and Future Directions in the Treatment of Hepatocellular Carcinoma*. *Gastroenterol Hepatol (N Y)*, 2017. **13**(7): p. 398-410.

51. Jansen, M.C., et al., *Outcome of regional and local ablative therapies for hepatocellular carcinoma: a collective review*. Eur J Surg Oncol, 2005. **31**(4): p. 331-47.
52. Weaver, M.S., S.C. Howard, and C.G. Lam, *Defining and distinguishing treatment abandonment in patients with cancer*. J Pediatr Hematol Oncol, 2015. **37**(4): p. 252-6.
53. Sippel, S., et al., *Review article: Use of ultrasound in the developing world*. Int J Emerg Med, 2011. **4**: p. 72.
54. Zhang, W.Y., Z.S. Li, and Z.D. Jin, *Endoscopic ultrasound-guided ethanol ablation therapy for tumors*. World J Gastroenterol, 2013. **19**(22): p. 3397-403.
55. Maza, M., et al., *Cervical Precancer Treatment in Low- and Middle-Income Countries: A Technology Overview*. J Glob Oncol, 2017. **3**(4): p. 400-408.
56. Kikinis, R., S.D. Pieper, and K.G. Vosburgh, *3D Slicer: a platform for subject-specific image analysis, visualization, and clinical support, in Intraoperative imaging and image-guided therapy*. 2014, Springer. p. 277-289.

Figures

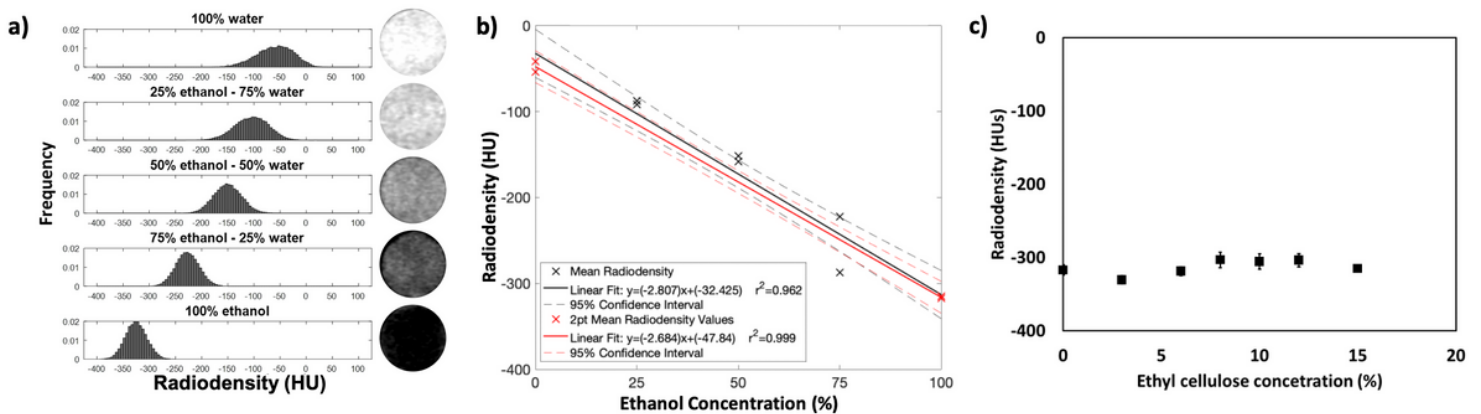


Figure 1

Measurement of ethanol concentration in water by computed tomography. a) Radiodensity distribution and cross-sectional images of 0%, 25%, 50%, 75%, and 100% ethanol-water solutions demonstrate that ethanol has endogenous CT contrast. b) Radiodensity values for ethanol-water solutions (n=2 for each concentration) from a representative imaging session fit using a linear fit and a 2-point linear calibration equation with 95% confidence intervals. c) Average radiodensity of EC-ethanol mixtures measured in triplicate. Error bars indicate standard deviation of average radiodensity value for a given EC concentration.

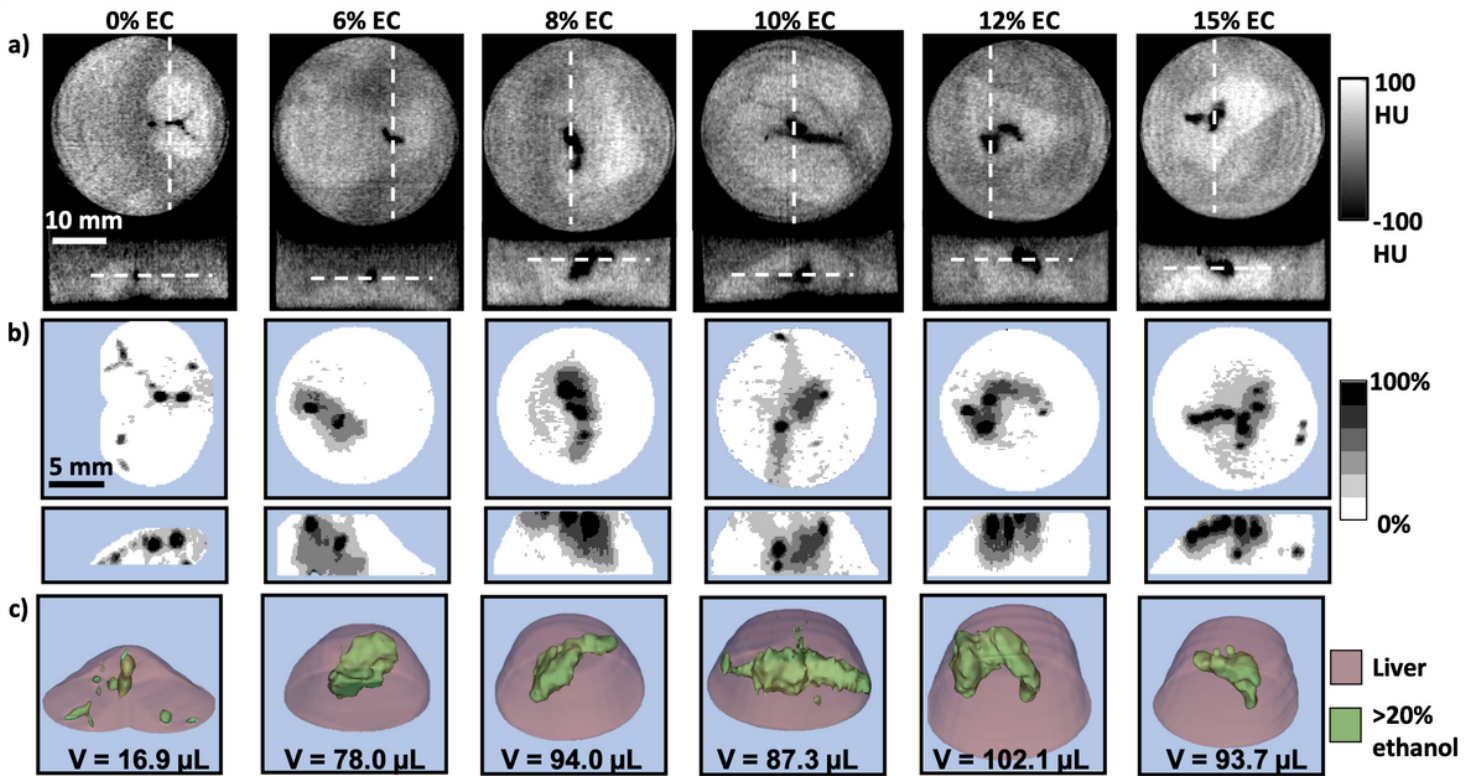


Figure 2

Visualizing the effect of EC concentration on injected ethanol distribution. a) Representative transverse (top) and frontal (bottom) cross-sections of CT images acquired 5 minutes after injection of EC-ethanol into the ex vivo rat liver. White dashed lines represent the plane of the accompanying image. 100 μL of EC-ethanol at 0%, 6%, 8%, 10%, 12%, or 15% EC was injected at 10 mL/h. Tissue was submerged in buffer to prevent air absorption that would artificially lower the radiodensity. b) Representative maximum concentration projections of transverse (top) and frontal (bottom) views, with the grayscale indicating 20% ethanol concentration bands. c) 3D segmentations of ethanol distributions at different EC concentrations with the volume of each segmentation denoted below. Green regions contain at least 20% ethanol, and the pink region corresponds to segmented liver.

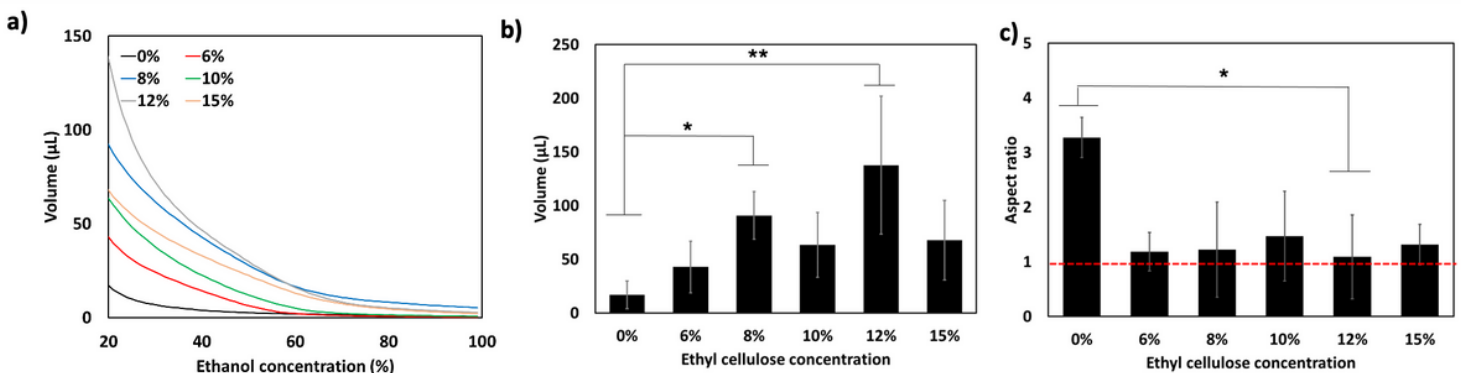


Figure 3

12% EC leads to the largest and most spherical ethanol distribution. a) Average cumulative volume histograms for each EC concentration. b) Volume and c) aspect ratio of the ethanol distribution. The red line denotes a spherical aspect ratio of 1, Error bars indicate standard deviation. * $p < 0.05$ and ** $p < 0.01$ (ANOVA and Tukey's test) versus 0% EC-ethanol ($n=6$ for each group).

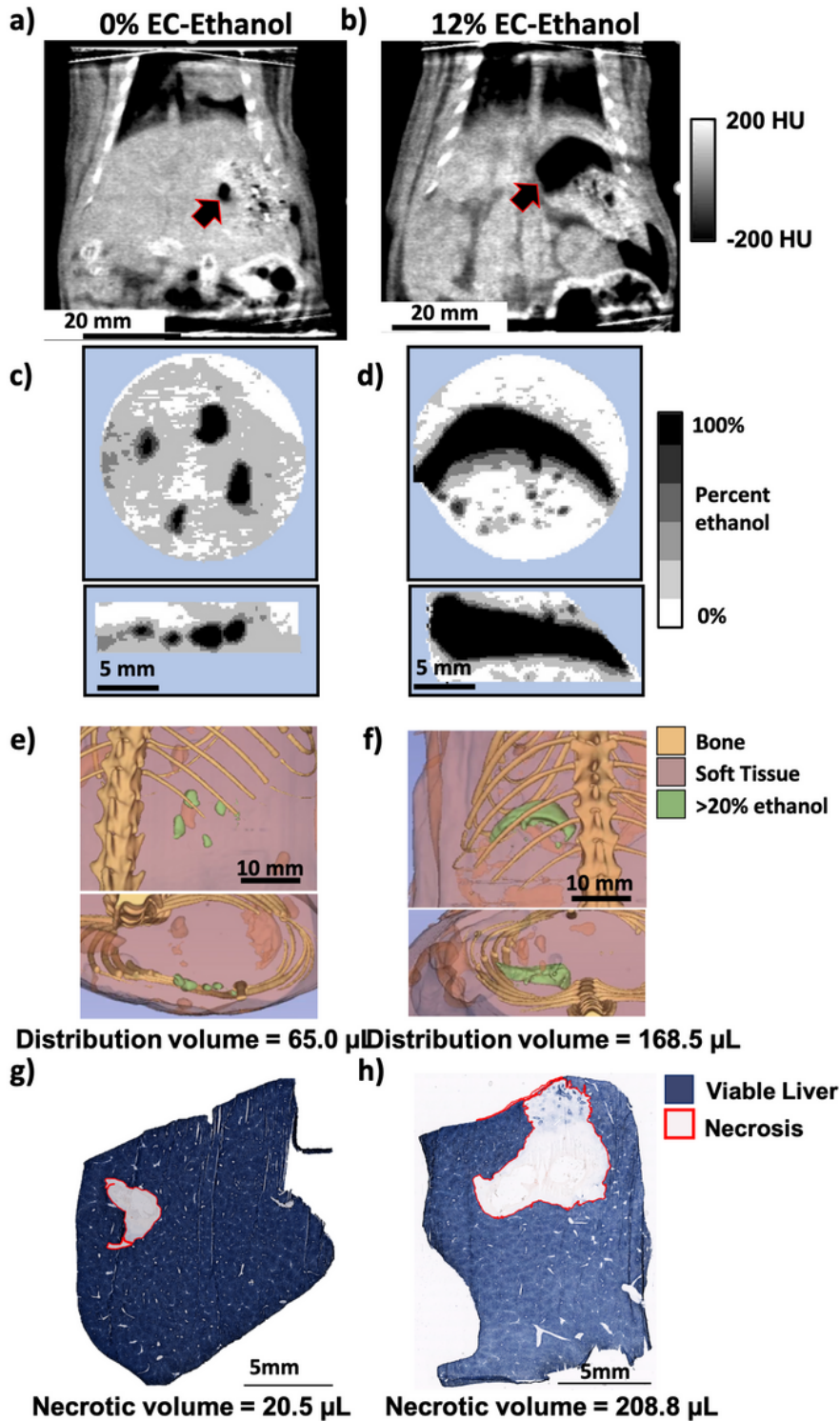


Figure 4

12% EC-ethanol improves localization and extent of ablation in rat liver in vivo. a-b) Representative frontal plane CT images showing ethanol distribution (arrow) for 0% and 12% EC-ethanol. c-d) Maximum intensity projections for the frontal (top) and transverse (bottom) views illustrate multiple foci of ethanol for 0% EC, and a single, large, connected distribution for 12% EC. e-f) 3D segmentations from a frontal plane (top) and transverse plane (bottom) for injections of pure ethanol into in vivo rat liver depict small and unconnected ethanol distributions. In contrast, the 3D segmentations from a frontal plane (top) and transverse plane (bottom) for 12% EC-ethanol demonstrate a larger and completely connected ethanol distribution. The distribution volume for each sample is quantified under each representative image. g) NADH-diaphorase viability staining of a representative section of tissue injected with pure ethanol shows a small area of necrosis (gray) surrounded by viable liver (blue). h) NADH-diaphorase viability staining of a representative section of tissue injected with 12% EC-ethanol shows a larger area of necrosis (gray, outlined in red) surrounded by viable liver (blue). The volume of induced necrosis is quantified under each representative image.

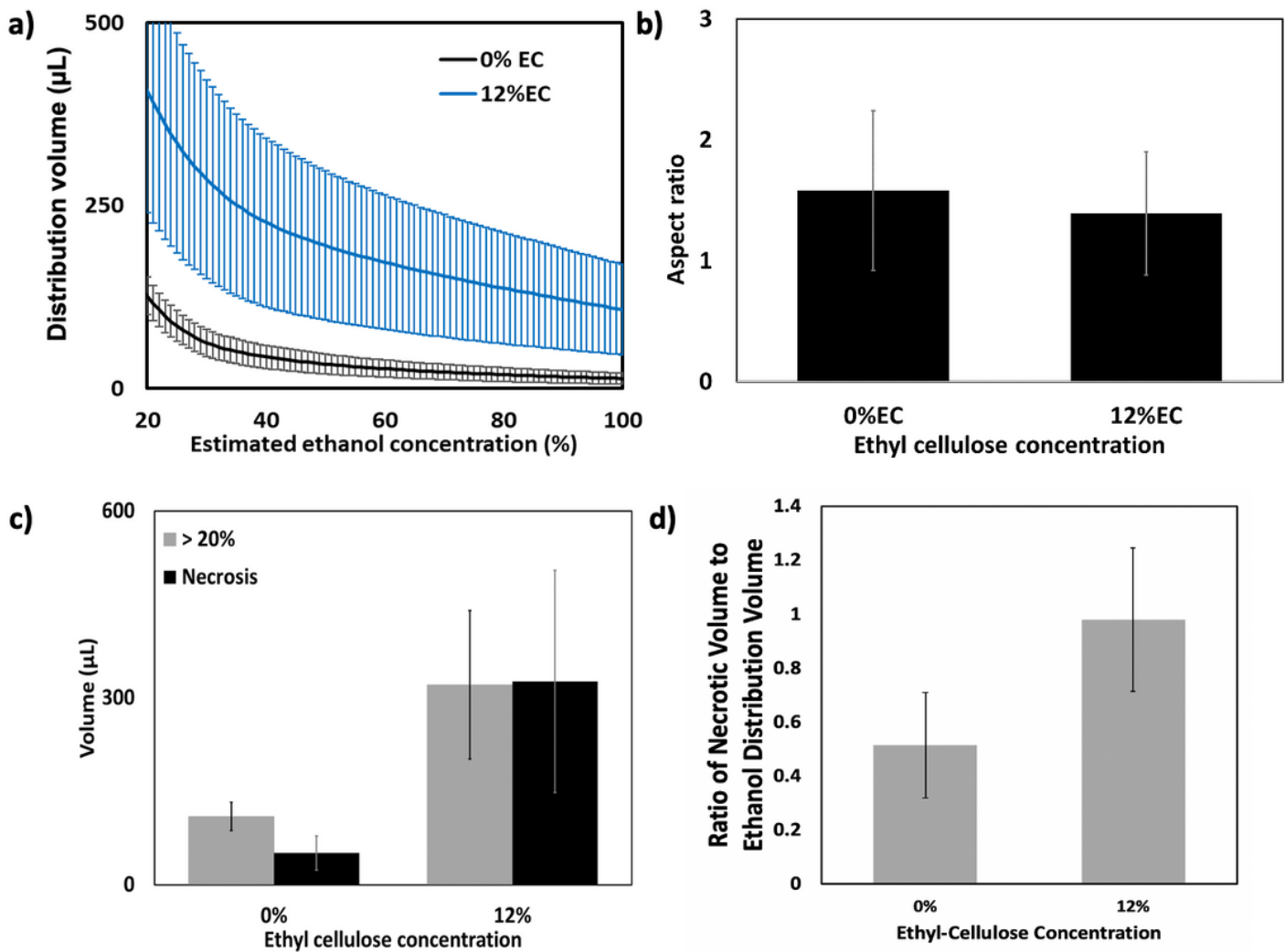


Figure 5

12% EC-ethanol improves localization of injected ethanol and effectiveness of ablation. a) Average cumulative volume histograms for the injection distribution volume corresponding to the estimated

ethanol concentration illustrate improved delivery for 12% EC-ethanol compared to pure ethanol. b) The aspect ratio for pure ethanol is higher than that of 12% EC-ethanol indicating that distributions are less spherical (N.S.) c) Both the volume of induced necrosis and the $\geq 20\%$ ethanol distribution volume are significantly greater for 12% EC-ethanol than for pure ethanol ($p < 0.05$, $n = 6$). d) The average ratio of the necrotic volume to ethanol distribution volume is closer to 1 for 12% EC than for pure ethanol (N.S.), indicating that CT imaging provides a more accurate prediction of necrosis for EC-ethanol than pure ethanol.

Supplementary Files

This is a list of supplementary files associated with this preprint. Click to download.

- [SupplementaryFigure1.tiff](#)
- [SupplementaryFigure2.tiff](#)
- [SupplementaryFigure3.tiff](#)
- [SupplementaryFigure4.tiff](#)
- [SupplementaryFigure5.tiff](#)
- [SupplementaryFigure6.tiff](#)
- [SupplementaryFigures.docx](#)